PCCP

ROYAL SOCIETY OF CHEMISTRY

PAPER

View Article Online
View Journal | View Issue

Cite this: *Phys. Chem. Chem. Phys.*, 2021, **23**, 19503

Phase transition and chemical reactivity of 1H-tetrazole under high pressure up to 100 GPa†

Dexiang Gao,[a] Xingyu Tang,[a] Xuan Wang,[a] Xin Yang,[a] Peijie Zhang,[a] Guangwei Che,[a] Jun Han,[a] Takanori Hattori,[b] Yajie Wang,[a] Xiao Dong,[c] Haiyan Zheng,*[a] Kuo Li[a] and Ho-kwang Mao[a]

Received 28th June 2021,
Accepted 10th August 2021

DOI: 10.1039/d1cp02913d

rsc.li/pccp

The pressure-induced phase transition and polymerization of nitrogen-rich molecules are widely focused on due to their extreme importance for the development of green high-energy-density materials. Here, we present a study of the phase-transition behaviour and chemical reaction of 1H-tetrazole up to 100 GPa using *in situ* Raman, IR, X-ray diffraction, neutron diffraction techniques and theoretical calculations. A phase transition above 2.6 GPa was identified and the high-pressure structure was determined with one molecule in a unit cell instead of two molecules as reported before. The 1H-tetrazole polymerized reversibly below 100 GPa, probably through carbon–nitrogen bonding instead of nitrogen–nitrogen bonding. Our studies update the structure model of the high-pressure phase of 1H-tetrazole, and present the possible intermolecular bonding route for the first time, which gives new insights to understand the phase transition and chemical reaction of nitrogen-rich compounds, and is of benefit for designing new high-energy-density materials.

Introduction

Synthesizing and recovering new polynitrogen materials has great significance for the development of green high-energy-density materials.[1] Applying extreme pressure on nitrogen-rich molecules is an efficient and powerful method for the development of high-energy-density materials. For example, various N_2 phases and poly-N_2 were obtained in a vast pressure–temperature (P–T) space by compressing N_2,[2–8] with amorphous polymeric nitrogen synthesized at 150 GPa and room temperature, "black nitrogen" at 146 GPa and 2200 K, *LP*-N at 120–180 GPa and 2000–3000 K, and *cg*-N at 110 GPa and 2000 K.[9–13] Despite large chemical energies and specific impulse being estimated for these poly-N_2 materials, their synthesis is still a huge challenge.[14,15] High-temperature and high-pressure conditions, typically over 100 GPa and 2000 K, are required, and the poly-N_2 materials become unstable when decompressed at room temperature, which restricts their application in practice.[13]

To decrease the reaction pressure and temperature, small molecules like CO, H_2O and H_2 have been introduced.[16–19] Doping with carbon and oxygen atoms has been reported to be effective to improve the stability of the polymeric product by releasing the strain of the chain or ring.[20,21] Yoo *et al.* evidenced that starting from a N_2–CO mixture, a high-density copolymer CON_2 could be synthesized at 45 GPa and 1700 K, which are lower than the conditions required for the synthesis of pure N_2 polymers.[22] A much lower synthetic pressure (6.9–26 GPa) was needed when the CO–N_2 mixture was irradiated by a laser, and the resulting extended material could be quenched down to 1–2 GPa.[23] By compressing a N_2–H_2 mixture, two stable high-pressure van der Waals compounds, $(N_2)_6(H_2)_7$ and $N_2(H_2)_2$, could be obtained below 10 GPa and an amorphous dinitrogen network was formed at 50 GPa.[24]

Another strategy to decrease the reaction pressure is to start from nitrogen-rich compounds. In contrast to N_2, these compounds often contain N=N double bonds, which are thought to be easier to polymerize. Here, 1H-tetrazole (H_2CN_4), with a high nitrogen content (80%) and good stability, is an ideal molecule to synthesize polynitrogen materials and the reaction mechanism has thus been investigated.[25] In the literature, 1H-tetrazole and its analogues have been investigated under high pressure, and polymorphs with high density and even polymerized structures were expected. Using *in situ* spectroscopy and X-ray diffraction, Li *et al.* reported a phase transition of 1H-tetrazole above 3 GPa and

[a] *Center for High Pressure Science and Technology Advanced Research, Beijing 100094, P. R. China. E-mail: zhenghy@hpstar.ac.cn*
[b] *J-PARC Center, Japan Atomic Energy Agency, Tokai, Ibaraki 319-1195, Japan*
[c] *Key Laboratory of Weak-Light Nonlinear Photonics, School of Physics, Nankai University, Tianjin 300071, P. R. China*

† Electronic supplementary information (ESI) available: Raman frequency shifts of 1H-tetrazole as a function of pressure (Fig. S1); IR frequency shifts of 1H-tetrazole as a function of pressure (Fig. S2); XRD patterns of the 1H-tetrazole recovered from high pressure (Fig. S3); Raman and IR spectra of the 1H-tetrazole recovered from 100.3 GPa (Fig. S4); the Rietveld refinement results of the XRD patterns of phase I at 0.3 GPa and phase II at 100.3 GPa (Fig. S5); optimized lattice parameters of phase I under high pressure (Fig. S6); atomic coordinates in phase II at 10 GPa (Table S1). Lattice parameters of phase II at 100.3 GPa and polymers obtained from XRD and simulation results, respectively (Table S2). See DOI: 10.1039/d1cp02913d

then an amorphization process followed at ~13 GPa.[26] A high-pressure phase (phase II) with a *P*1 space group and a dimer-like structure was proposed. Jin *et al.* studied 1,5-diamino-1*H*-tetrazole under high pressure and reported a more complex phase-transition process. These phase transitions were evidenced to be related to the rotation of NH_2 and the distortion of the heterocycle, which was induced by the hydrogen bond reconstitution.[27] For 1-methyl-5-nitramino-1*H*-tetrazole, molecular distortions and structural modifications were observed in the crystal as the pressure increased and no phase transition occurred below 40 GPa.[28] Up to now, most of the literature reports are about the phase transition processes. We still lack knowledge about the crystal structures and the chemical reactions under high pressure. In this work, we investigated the structure evolution and chemical reaction of 1H-tetrazole up to 100 GPa by using multiple experimental and theoretical methods, and then re-determined and updated the crystal structure of phase II by the *in situ* synchrotron X-ray and neutron diffractions. We found that 1H-tetrazole experienced a reversible chemical reaction below 100 GPa, and proposed an intermolecular C···N bonding route instead of N···N bonding and hence obtained the primary product models. Our studies systematically investigated the structure evolution and polymerization process of 1H-tetazole up to 100 GPa, providing new insights for designing and synthesizing new nitrogen-rich materials under high pressure.

Experimental

The 1H-tetrazole (98%, Innochem) used for Raman, IR and synchrotron X-ray diffraction (XRD) measurements was well grounded and loaded in to diamond anvil cells. Symmetric diamond anvil cells with a culet of d = 300 μm and d = 250 μm were used for high-pressure spectral and X-ray diffraction measurements, respectively. T-301 stainless steel gaskets with a thickness of 30 μm and a 120 μm diameter hole at the centre were used for the sample chamber. *In situ* Raman spectra were measured on a Renishaw Raman microscope with excitation laser wavelength at 532 nm. For the IR experiments, a pair of type II diamonds was used. *In situ* IR spectra were collected on a Bruker VERTEX 70v with a HYPERION 2000 microscope and Globar as a conventional source, and the collection range was 600–4000 cm^{-1} with a resolution of 2 cm^{-1} in transmission mode. No pressure medium was used and the ruby fluorescence was used to calibrate the pressure.[29]

In situ high-pressure angle-dispersive X-ray diffraction experiments were performed at the 4W2 beamline of Beijing Synchrotron Radiation Facility (BSRF) and 15U1 beamline of Shanghai Synchrotron Radiation Facility (SSRF). The wavelength of incident monochromatic X-ray was 0.6199 Å and the distance between the sample and detector was calibrated by a CeO_2 standard sample. The beam sizes were ~20 × 30 and 2 × 2 μm^2, respectively. Dioptas software was used to reduce the collected data.[30]

The deuterated tetrazole for the neutron diffraction experiments was prepared by heating the solution with a mass ratio of 1H-tetrazole and D_2O of 1 : 3.5 under reflux for 48 h and then removing the D_2O under freeze-drying conditions. The hydrogen on N was deuterated while that on C was not, according to the ref. 31. *In situ* high-pressure neutron diffraction was measured on a J-PARC BL11 system (PLANET).[32] A Paris–Edinburgh press VX4 was used to provide high pressure and Ti–Zr alloy gaskets were used as the sample chamber. Sintered diamond double toroidal anvils were used for the experiments. The calibration curve of the instrument was used to calibrate the pressure.[33] The data were collected from ambient pressure to 14 GPa. The collected d ranges were 0–8.4 Å below 10 GPa and 0–4.2 Å above 10 GPa, respectively. The collection time at one pressure point was 5 h. The Jana 2006 package was used to perform the Rietveld refinement.[34]

Density-functional theory (DFT) calculations were performed with the generalized gradient approximation (GGA)[35] exchange–correlation functional in the CASTEP module of Material Studio.[36] Structure optimization was carried out first to explore the properties and behaviours of 1H-tetrazole under high pressure. Simulated IR and Raman spectra[37] were then calculated for the reference. Finally, molecular dynamics (MD) simulations were performed to explore the potential reactions in this system within an *NPT* ensemble at 100 GPa and 400 K.[38,39] Norm-conserving pseudopotentials[40] and an energy cut-off for the plane wave basis set at 570 eV were implemented in all the calculations above with the k-points sampling resolution being 0.04 × 2π $Å^{-1}$. Besides, to take the non-covalent interaction into consideration, DFT-D correction developed by Tkatchenko and Scheffler[41] was applied to our system.

Results and discussion

Raman spectra under high pressure

Fig. 1 displays the Raman spectra of 1H-tetrazole up to 47 GPa without a pressure-transmitting medium. All the vibration modes at 0.6 GPa were assigned according to the theoretical calculation results (Table 1). With increasing pressure, all the

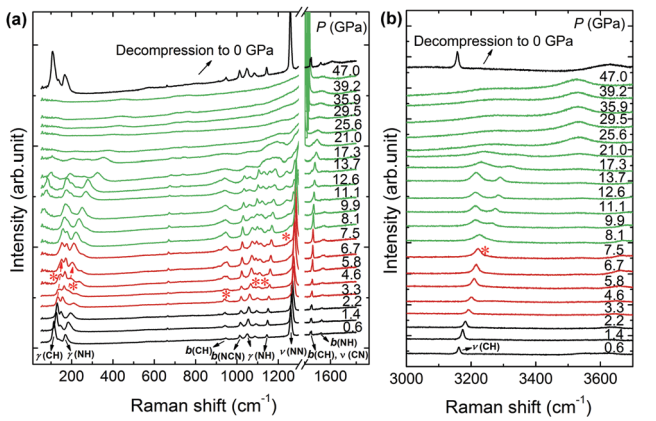

Fig. 1 Raman spectra of 1H-tetrazole under non-hydrostatic pressure up to 47 GPa in the region of (a) 50–1700 cm^{-1} and (b) 3000–3700 cm^{-1}. The new peaks are marked by asterisks. The dash lines represent the blueshift of the lattice vibration mode of phase II. γ represents out-of-plane bending vibration; ν represents stretching vibration; b strands for in-plane bending vibration.

Table 1 Assignments of the Raman modes of 1H-tetrazole at 0.6 GPa and room temperature

Assignments	Experiment (cm^{-1})	Calculation (cm^{-1})
γ (C–H)	113	131
γ (ring)	136	154
γ (C–H), γ (N–H)	170	185
γ (C–H)	661	663
b (C–H)	946	932
b (N–C–N)	1013	1000
ν (N–N)	1050	1051
ν (N–N), b (C–H)	1088	1074
ν (N–N), b (C–H)	1144	1123
ν (N–C–N), b (N–H)	1260	1256
ν (C–N), b (C–H)	1443, 1451	1423
ν (C–N), b (N–H)	1526	1547
ν (C–H)	3162	3204

Note: γ represents out-of-plane bending; ν represents stretching; b stands for in-plane bending.

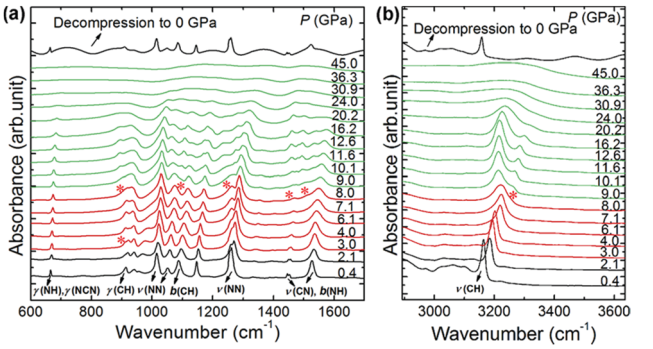

Fig. 2 IR spectra of 1H-tetrazole under non-hydrostatic pressure up to 45.0 GPa in the region of (a) 600–1700 cm^{-1} and (b) 2900–3620 cm^{-1}. The new peaks are marked by asterisks. γ represents out-of-plane bending; ν represents stretching; b stands for in-plane bending.

Raman modes shifted to high frequency slowly (frequency shifts plot shown in Fig. S1, ESI†). As shown in Fig. 1a, at 3.3 GPa, the peak at 954 cm^{-1}, marked by asterisks (bending mode of the C–H bond), split. At 4.6 GPa, a new lattice vibration mode at 187 cm^{-1} appeared while new peaks emerged at 1085 and 1136 cm^{-1} in the region of ring bending and stretching. This indicated the onset of the transition from phase I to phase II. Upon compression up to 6.7 GPa, the peaks at 187, 1085 and 1136 cm^{-1} assigned to phase II were gradually enhanced and the lattice vibration modes (below 200 cm^{-1}) of phase I gradually disappeared. Above 7.5 GPa, in the lattice vibration region, only four peaks of phase II were present and two new peaks emerged at 1257 and 3250 cm^{-1}, which indicated the ending of the phase transition. With increasing pressure up to 47 GPa, all the peaks were blueshifted and gradually disappeared without any appearance of new peaks. After decompressing to ambient pressure, several peaks of phase I appeared again, indicating that 1H-tetrazole underwent a reversible phase-transition process and no chemical reactions occurred under a pressure of up to 47 GPa.

IR spectra under high pressure

Fig. 2 displays the IR spectra of 1H-tetrazole under non-hydrostatic pressure conditions up to 45.0 GPa (frequency shifts of the IR modes are shown in Fig. S2, ESI†). As shown in Fig. 2a, a shoulder peak at 910 cm^{-1} emerged at 3 GPa, indicating the onset of the transition process from phase I to phase II. At 8.0 GPa, several new peaks appeared at 903, 1085, 1251, 1460 and 1506 cm^{-1} in the region of ring vibration. Upon further compression up to 45 GPa, all the peaks shifted and broadened while no new peaks could be observed. This suggests that the phase transition from I to II was completed at 8 GPa, in agreement with the Raman results. After decompression, all the peaks of phase I emerged again, which also demonstrated that the phase-transition process was reversible.

In situ X-ray and neutron diffraction under high pressure

To investigate the structural evolution in the phase-transition process, *in situ* high-pressure X-ray diffraction (XRD) patterns of 1H-tetrazole under non-hydrostatic pressure conditions were collected up to 100.3 GPa. As shown in Fig. 3a, in the first run, all the peaks are shifted to a high angle upon compression. Above 2.6 GPa, two new diffraction peaks emerge at the high-angle side of the 010 peak and the low-angle side of the 100 peak, respectively. This is attributed to the emergence of phase II, consistent with the spectroscopic results. From 2.1 GPa to 7.4 GPa, the diffraction peaks of phase I, such as 010, 001 and 100, are gradually weakened, while those of phase II are enhanced. At 7.4 GPa, all the diffraction peaks are ascribed to phase II, and the profile is similar to that of phase I, including the distribution of the peaks and the relative intensities. This suggests that the crystal structure of 1H-tetrazole did not change significantly upon compression, including the molecular geometry and the stacking. With increasing pressure, all the diffraction peaks were still observable up to 60.0 GPa, confirming the stability of phase II. When decompressed from 60.0 GPa, the XRD pattern was the same as that at ambient pressure (Fig. S3, ESI†), still demonstrating a reversible phase-transition process in the compression–decompression cycle up to 60 GPa. The phase transition from I to II could also be observed in the *in situ* high-pressure neutron diffraction patterns (Fig. 3b), with two new diffraction peaks emerging above 3 GPa and 5 GPa, respectively (asterisks in Fig. 3b). The profile above 8 GPa was also similar to that of phase I.

In the second XRD run (Fig. 3a), we compressed the sample up to 100.3 GPa. The diffraction patterns were still similar to those below 60 GPa, but with the peaks more broadened. All the diffraction peaks shifted to a higher angle slowly and were still observable up to 100.3 GPa, in contrast with the amorphization above 13 GPa reported in the literature.[26] When decompressed to ambient pressure, the XRD pattern only contained a broad diffraction peak in the range of 8°–9°, which was different from that of phase I at ambient pressure. This means that the 1H-tetrazole crystal underwent an irreversible process in the pressure range from 60 to 100.3 GPa. Besides, a strong fluorescence background and weak peaks existed in the Raman spectra of the recovered sample from 100.3 GPa, which also suggested an irreversible process (Fig. S4a, ESI†). However, even if something irreversible occurs, the recovered sample from 100.3 GPa was mainly 1H-tetrazole according to its IR spectra (Fig. S4b, ESI†). Combined with the theoretical calculation results shown below,

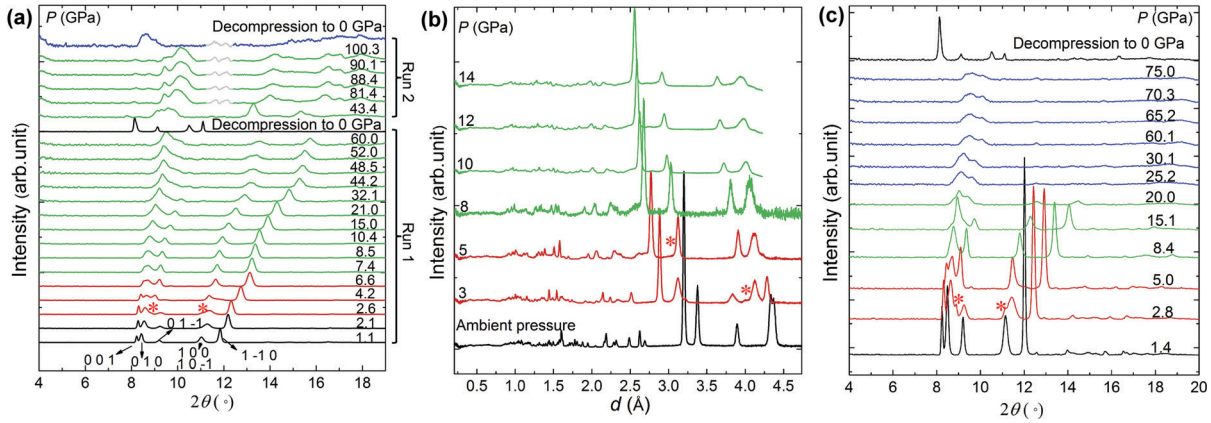

Fig. 3 (a) Selected XRD patterns of 1H-tetrazole up to 60 GPa (Run 1) and 100 GPa (Run 2) without shear. (b) Neutron diffraction patterns of 1D-tetrazole up to 14 GPa. (c) Selected XRD patterns of 1H-tetrazole up to 75 GPa with shear. The new diffraction peaks are marked by asterisks. The peaks from the Kikuchi band of diamond are masked by grey lines in (a).

this suggests a reversible chemical reaction occurred in this compression–decompression process, which disturbed the lattice significantly while the molecules recovered.

Additionally, another structural evolution process was observed during compression. In the third XRD run, the hole of gasket gradually expanded and deformed with the increasing pressure, resulting in a shear deformation of the sample. As shown in Fig. 3c, the same phase-transition process from I to II occurred below 8.4 GPa, while above 20 GPa, the diffraction peaks above 11° (100, 10$\bar{1}$, 1$\bar{1}$0) nearly disappeared and only two peaks (010, 001) at 9° survived up to 75.0 GPa. The disappearance of the diffraction peaks hkl ($h \neq 0$) indicated that the orderly stacking of molecules along the *a*-axis partly collapsed. Similar XRD patterns were also reported in ref. 26 where the amorphization process was proposed to start above 13 GPa. In this work, we found that the 1H-tetrazole recovered from 75.0 GPa displayed the same XRD peak positions as that at ambient pressure but with different intensities (Fig. S3, ESI†). Thus, we can conclude that the shear deformation leads to deterioration of the crystal quality, enhances the orientation above 20 GPa, and affects the phase-transition process of the tetrazole, but does not cause irreversible changes in the crystal structure.

Structure analysis under compression

The crystal structures of 1H-tetrazole under high pressure were determined by performing Rietveld refinement. For phase I, the structural model of 1H-tetrazole used for refinement was taken from ref. 42.[42] The refined lattice parameters of phase I at 0.3 GPa are shown in Table 2, with the Rietveld refinement plot shown in Fig. S5 (ESI†), which only showed tiny changes compared to the reference. For phase II, the XRD peaks showed a similar distribution and relative intensities with that of phase I, so we indexed the peaks using the same diffraction indexes (010, 001, 01$\bar{1}$, 10$\bar{1}$, 100 and 1$\bar{1}$0) of phase I. The lattice parameters were then calculated manually and refined (Rietveld refinement plot shown in Fig. 4a). The refined lattice parameters of phase II at 8.4 GPa are shown in Table 2. In the refinements, the 1H-tetrazole molecule (with hydrogen for phase I and without hydrogen for phase II) was restrained as a rigid body to decrease the degree of freedom, and all the peaks of the XRD patterns could be well fitted. The atomic coordinates of phase II at 8.4 GPa are listed in Table 3.

Table 2 Lattice parameters of phase I and phase II

	Phase I (0.3 GPa, XRD)	Phase II (8.4 GPa, XRD)	Phase II (10 GPa, neutron)
a (Å)	3.734 (1)	3.259 (1)	3.249 (2)
b (Å)	4.782 (1)	4.534 (1)	4.435 (3)
c (Å)	4.927 (2)	4.738 (2)	4.697 (6)
α (°)	107.14 (1)	113.90 (3)	113.22 (9)
β (°)	107.17(2)	110.37 (3)	111.41 (11)
γ (°)	101.57(2)	90.75 (2)	90.46 (6)
V (Å^3)	76.23 (4)	59.04 (3)	56.99 (12)
Space group	*P*1	*P*1	*P*1

To determine the positions of the hydrogen atoms, Rietveld refinement was also performed on the neutron diffraction pattern of phase II (deuterated) collected at 10 GPa. The pattern could be best fitted when deuterium is bonded to N1 (Rietveld refinement plot in Fig. 4b). The refined lattice parameters and atomic coordinates of phase II at 10 GPa are shown in Table 2 and Table S1 (ESI†).

The lattice parameters as a function of pressure are shown in Fig. 5a, with the *a*-axis showing the maximum compression, while the unit cell volumes below 25.8 GPa were fitted by using the third-order Birch–Murnaghan equation of state:[43,44]

$$P(V) = 1.5B_0\left[\left(\frac{V_0}{V}\right)^{\frac{7}{3}} - \left(\frac{V_0}{V}\right)^{\frac{5}{3}}\right] \times \left\{1 + \frac{3}{4}(B_1 - 4)\left[\left(\frac{V_0}{V}\right)^{\frac{2}{3}} - 1\right]\right\}$$

where V_0 is the unit cell volume at ambient pressure, and B_0 and B_1 are the isothermal bulk modulus and its first pressure derivative. As shown in Fig. 5b, two curves were used to fit the data from two phase regions with B_1 fixed to 4, respectively. For phase I, $V_0 = 75.6 \pm 0.4$ Å^3, $B_0 = 13.6 \pm 0.9$ GPa. For phase II, $V_0 = 67.5 \pm 0.4$ Å^3, $B_0 = 45.7 \pm 1.5$ GPa.

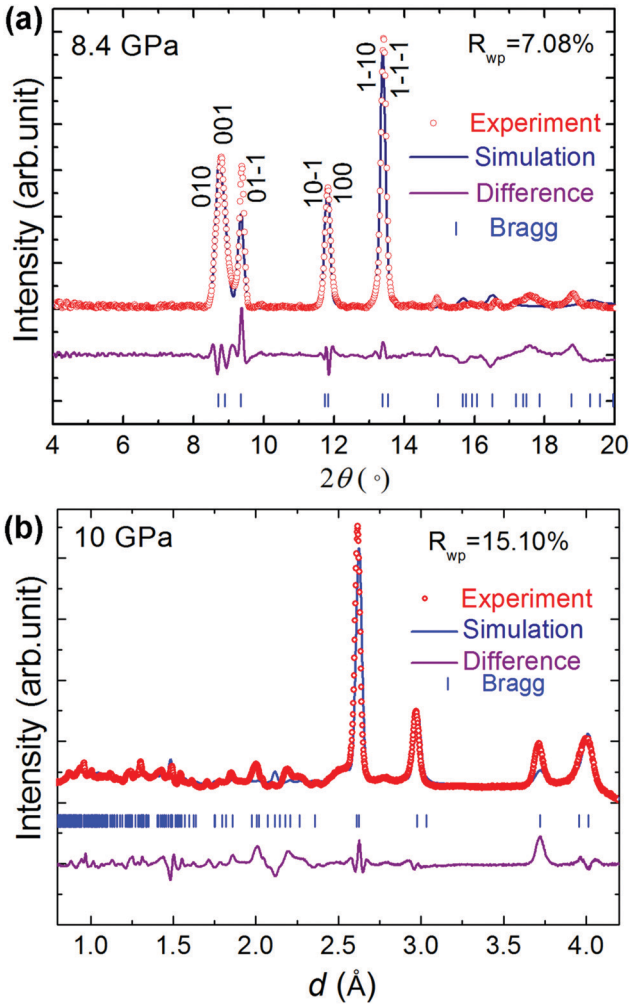

Fig. 4 Results from the Rietveld refinement of the XRD patterns of (a) phase II at 8.4 GPa and neutron diffraction patterns of (b) phase II at 10 GPa. All the diffraction peaks could be well fitted with R_{wp} = 7.08% and R_{wp} = 15.10%, respectively.

Table 3 Atomic coordinates in phase II at 8.4 GPa

Label	*x*	*y*	*z*
N1	0.1163	0.1263	0.8315
N2	0.3828	0.3818	0.8722
N3	0.3777	0.3601	0.6017
N4	0.1124	0.0943	0.3878
C5	−0.0450	−0.0460	0.5393

Note: the uncertainty of the atomic coordinates is not provided by the software under the rigid body restrictions.

The crystal structures of phase I at 0.3 GPa and phase II at 8.4 GPa are shown in Fig. 6a and b, respectively. In phase I, each 1H-tetrazole molecule connects to six adjacent molecules by hydrogen bonds, with the distances between N1(H)···N4, C5(H)···N2 and C5(H)···N3 being 2.80, 3.32 and 3.39 Å, respectively. The structure of phase II remains in a similar stacking mode as shown in Fig. 6b, where the distances between N1···N4, C5···N2 and C5···N3 are 2.70, 3.05 and 3.43 Å, respectively. The distance between the molecules along the diagonal, C5···N2, decreases from 3.32 Å to 3.05 Å while N1···N3 increases from 6.78 Å to 6.88 Å. The hydrogen network transformed from a parallelogram shape in phase I (red dashed line in Fig. 6a) to two triangles (red dashed line in Fig. 6b) in phase II, with the significant compression of the C5···N2 distance. This is the main reason for the phase transition.

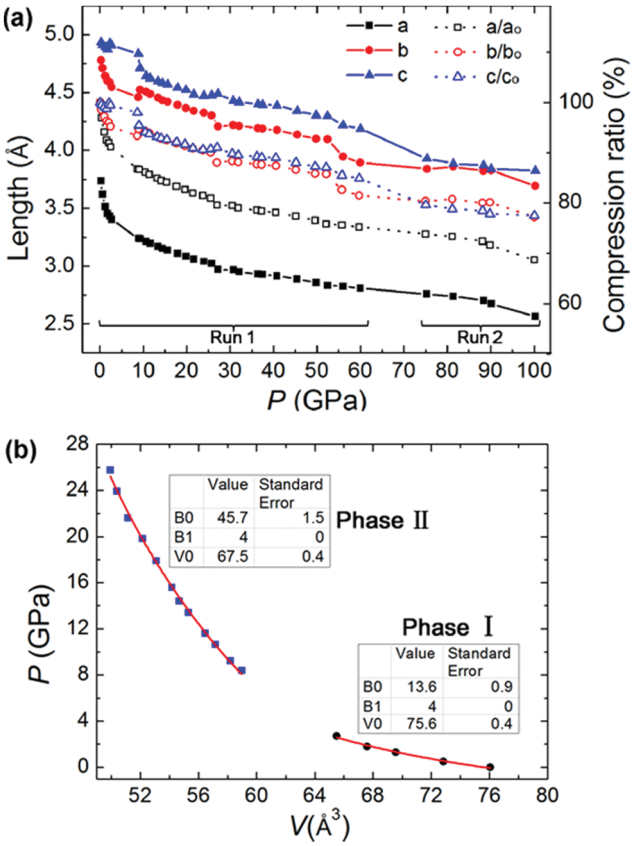

Fig. 5 (a) Variations in the cell parameters as a function of the pressure (solid lines) and compression ratio of three axes (dotted lines). (b) Birch–Murnaghan equation of the state of 1H-tetrazole under non-hydrostatic pressure conditions.

Note, the crystal of phase II described above only contained one 1H-tetrazole, in contrast to the literature which showed two non-equivalent molecules in the unit cell.[26] This can be confirmed by the theoretical calculation further. When we optimized the structural model of phase I from ambient pressure to 8 GPa, the optimized lattice parameters above 4 GPa (Fig. S6, ESI†) obviously changed, which is different from the structure reported in ref. 26 but similar to this new structure model. Besides, we also performed geometry optimizations on both the structure reported by Li *et al.* and the structure described in our manuscript. With optimizing the lattice parameters, under 8.4 GPa, the enthalpy of the new model (−1291.704 eV) was lower than the very dense structure reported by Li *et al.* (−1291.663 eV). Additionally, it was noteworthy that the interplanar distance underwent a significant compression, from 3.35 Å at 0.3 GPa to 2.65 Å at 8.4 GPa, just like other π-stacked layered crystals. This interplanar distance was much larger than the 2.16 Å (7.8 GPa) shown in the dimmer structure reported in the literature.[26]

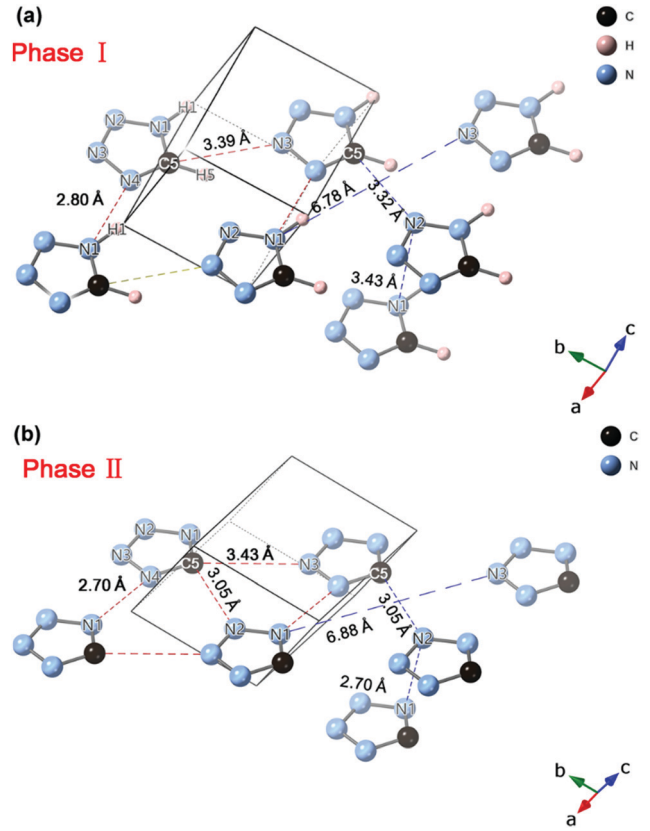

Fig. 6 Crystal structure of 1H-tetrazole for (a) phase I at 0.3 GPa and (b) phase II at 8.4 GPa.

For comparison, the interlayer distances of graphite at ambient pressure and 9.9 GPa were 3.35 Å and 2.99 Å, respectively.[45] For the C_6H_6–C_6F_6 co-crystal at ambient pressure and 20.0 GPa, the interlayer distances were 3.62 Å and 2.75 Å, respectively.[46,47] Thus, it seems that the interplanar distance of 2.65 Å at 8 GPa in the current work is more consistent with other aromatics, while the interlayer distance in the high-pressure phase reported in ref. 26 (2.16 Å) was too close to be reached at 7.8 GPa.

Theoretical calculations under high pressure

To investigate the bonding mechanism, the geometry optimization of 1H-tetrazole under 100 GPa was performed based on the structure obtained from the XRD results at 100.3 GPa (Table S2, ESI†), and the optimized lattice parameters (polymer 1) are shown in Table S2 (ESI†). The optimized result shows that a new covalent bond was formed between C5 and N3 in the adjacent molecule along the *b*-axis, and H1 transferred from N1 to N4, with H1···N1 at 1.37 Å and N4–H1 at 1.09 Å (Fig. 7a). This shows that 1H-tetrazole can polymerize at 100 GPa, with the product referred to here as polymer 1. The observed hydrogen transfer is obviously the requirement for the valence state. In polymer 1, N4 cannot form double bonds with C5 or N3, and must connect to H1 to satisfy the valence. When we started from the structural model of phase II at 8.4 GPa and optimize it at 100 GPa, polymer 1 could also be obtained. This confirmed the result and excluded the possible interference from the starting model. Thus, we can conclude that

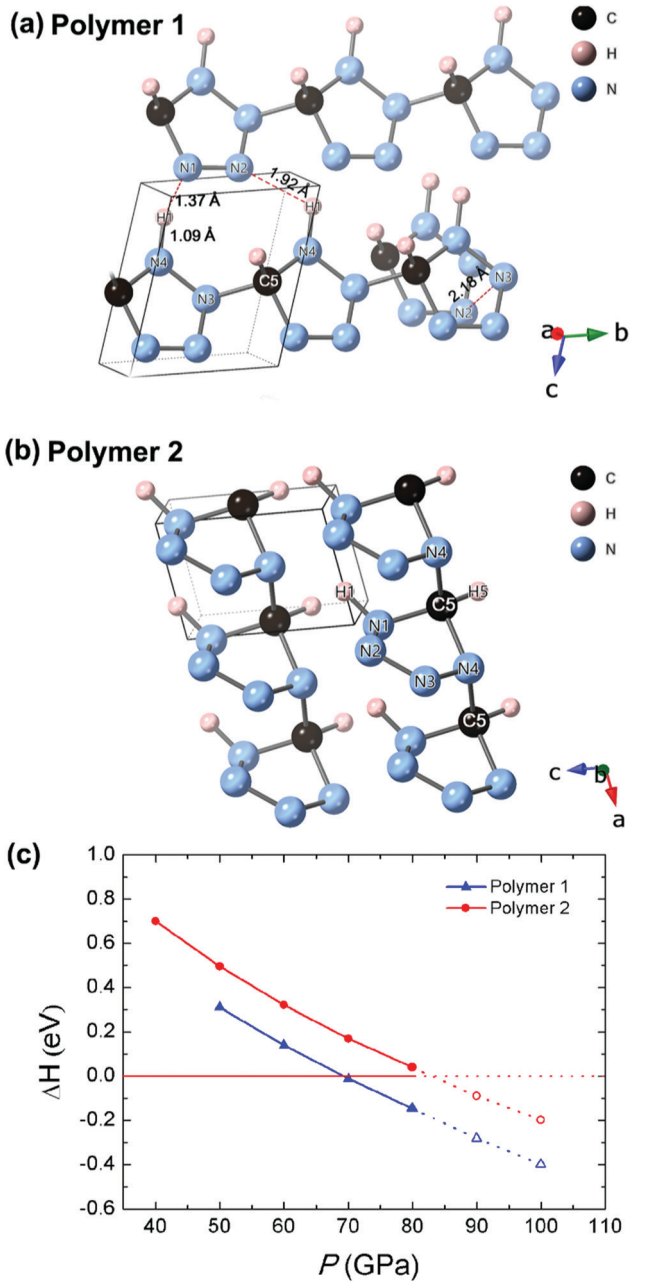

Fig. 7 Polymeric structures of 1H-tetrazole under 100 GPa. (a) Polymer 1, optimized from the structure obtained from the XRD result at 100.3 GPa, (b) Polymer 2, optimized from the dynamic calculation results under 100 GPa and 400 K. (c) The enthalpy differences between the polymers and the molecular crystal optimized starting from phase II at 8.4 GPa (red line at ΔH = 0). Above 80 GPa, extrapolated values are presented by a dotted line because the molecular phase could not maintain.

at 100 GPa the 1H-tetrazole molecules were not thermodynamically stable, and chemical reactions were highly likely to occur. Polymer 1 was stable down to 50 GPa in the optimization, and decomposed into 1H-tetrazole molecules at 40 GPa. This reversible process is consistent with the conclusion from the IR experiment, and suggested that the reaction of 1H-tetrazole is possible above 50 GPa, where both the Raman and IR spectra were already featureless.

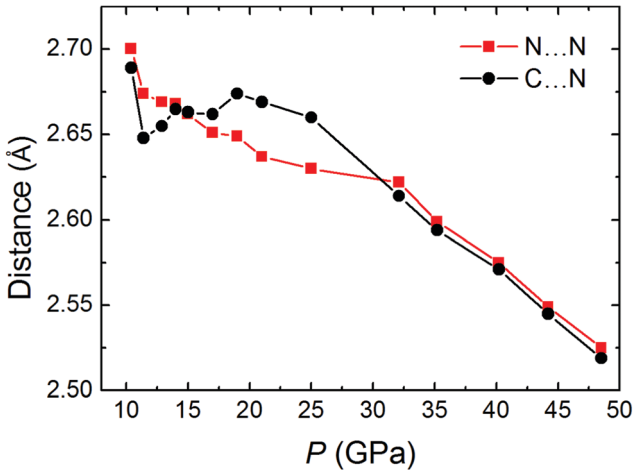

Fig. 8 Closest intermolecular N···N and C···N distance in adjacent layers as a function of pressure. Above 50 GPa, the spectra were already featureless. The lattice could still be obtained but the intermolecular distances were hard to be determined due to the data quality.

Starting from the model obtained by XRD at 100 GPa, a new polymeric structure was also observed *via* dynamic simulations under 100 GPa and 400 K (polymer 2, Fig. 7b), and its optimized lattice parameters are shown in Table S2 (ESI†). For polymer 2, C5 bonded to N4 along the *a*-axis, also between C and N instead of N and N. The polymeric structure was stable in the optimization down to 40 GPa, but decomposed into 1H-tetrazole molecules at 30 GPa. The enthalpies of the polymers are shown in Fig. 7c in comparison with the optimized molecular 1H-tetrazole crystal. Both polymers 1 and 2 have lower enthalpies compared to the molecular phase above 70–90 GPa. This clearly indicated that the polymerization was preferred and hence explained the reversible chemical reaction experimentally observed.

The simulation indicated that intermolecular bonding always forms between C and N, which implies it is extremely difficult to bond aromatic N atoms to form N–N bonds. For the unsaturated carbon-based molecules, like phenyl and alkynyl,[48–50] when the intermolecular distance between the carbon atoms is compressed to a certain distance at 2.8–3.0 Å at room temperature, the atoms will bond. This provides an experiential rule to design and synthesize new carbon materials. Here, in contrast, the critical distance for the reaction between aromatic nitrogen remained a mystery. As shown in Fig. 8, at 48.5 GPa, where the Raman and IR spectra were already featureless, the closest intermolecular N···N distance was 2.52 Å, which was still not enough to induce N–N bonding and hence this could be referred to as an upper limit for the critical distance. For comparison, the closest intermolecular C···N distance was also 2.52 Å, which suggests the bonding between C and N atoms is easier than N–N bonding.

Conclusions

In conclusion, 1H-tetrazole transfers to a new phase from 2.6 to 7.4 GPa and experiences a reversible chemical reaction process in the compression–decompression cycle up to 100 GPa. The *in situ* X-ray and neutron diffraction analyses showed that the high-pressure molecular phase had a *P*1 space group with one molecule in a unit cell, instead of two molecules as reported before. The theoretical investigation showed the reversible polymerization observed in the experiment was related to the formation of a new covalent bond between C and N atoms in neighbouring molecules, instead of between N atoms. Combined with the crystallographic research, we found at least 2.52 Å was not short enough to induce the bonding between the aromatic nitrogen atoms. This distance was much shorter than that of carbon analogues, and hence suggests a much tough condition is needed for nitrogen–nitrogen bonding. Our work systematically investigated the structure evolution and chemical reaction process of 1H-tetrazole, a typical nitrogen-rich molecule, and provides an important reference for understanding the reactivity of nitrogen-rich compounds, which will benefit the synthesis of new high-energy-density materials.

Author contributions

The D. Gao performed the experiments and theoretical calculations, wrote the original draft. X. Tang and X. Dong helped to analyze the calculation results. X. Wang, X. Yang, P. Zhang, G. Che, and Y. Wang helped to collect the XRD data. J. Han helped to synthesize the deuterated tetrazole. T. Hattori helped to perform the *in situ* neutron diffraction. H. Zheng and K. Li led the entire experiment, data analysis, and manuscript writing. H.-k. Mao led the funding acquisition. All authors approved the final version of the manuscript.

Conflicts of interest

There are no conflicts to declare.

Acknowledgements

This work was supported by the National Natural Science Foundation of China (NSFC) (Grant No. 21771011, 21875006 and 22022101). *In situ* high-pressure angle-dispersive X-ray diffraction experiments were performed at 4W2 beamline of Beijing Synchrotron Radiation Facility (BSRF) and 15U1 beamline of Shanghai Synchrotron Radiation Facility (SSRF). *In situ* high-pressure neutron diffraction experiments were performed through the J-PARC user programs (No. 2020B0448). The authors thank Dr Dongliang Yang and Dr Chengwen Mao for supporting the *in situ* X-ray diffraction measurements under high pressure.

Notes and references

1 K. O. Christe, *Propellants. Explos. Pyrotech.*, 2007, **32**, 194–204.
2 E. Gregoryanz, A. F. Goncharov, C. Sanloup, M. Somayazulu, H. K. Mao and R. J. Hemley, *J. Chem. Phys.*, 2007, **126**, 184505.
3 G. W. Stinton, I. Loa, L. F. Lundegaard and M. I. McMahon, *J. Chem. Phys.*, 2009, **131**, 104511.

4 R. Bini, L. Ulivi, J. Kreutz and H. J. Jodl, *J. Chem. Phys.*, 2000, **112**, 8522–8529.
5 R. Reichlin, D. Schiferl, S. Martin, C. Vanderborgh and R. L. Mills, *Phys. Rev. Lett.*, 1985, **55**, 1464–1467.
6 E. Gregoryanz, A. F. Goncharov, R. J. Hemley, H. K. Mao, M. Somayazulu and G. Y. Shen, *Phys. Rev. B: Condens. Matter Mater. Phys.*, 2002, **66**, 224108.
7 M. Scheerboom and J. A. Schouten, *Phys. Rev. Lett.*, 1993, **71**, 2252–2255.
8 R. D. Etters, V. Chandrasekharan, E. Uzan and K. Kobashi, *Phys. Rev. B: Condens. Matter Mater. Phys.*, 1986, **33**, 8615–8621.
9 A. F. Goncharov, E. Gregoryanz, H. K. Mao, Z. Liu and R. J. Hemley, *Phys. Rev. Lett.*, 2000, **85**, 1262–1265.
10 C. Ji, A. A. Adeleke, L. Yang, B. Wan, H. Gou, Y. Yao, B. Li, Y. Meng, J. S. Smith, V. B. Prakapenka, W. Liu, G. Shen, W. Mao and H. K. Mao, *Sci. Adv.*, 2020, **6**, eaba9206.
11 D. Tomasino, M. Kim, J. Smith and C. S. Yoo, *Phys. Rev. Lett.*, 2014, **14**, 205502.
12 M. J. Lipp, J. P. Klepeis, B. J. Baer, H. Cynn, W. J. Evans, V. Iota and C. S. Yoo, *Phys. Rev. B: Condens. Matter Mater. Phys.*, 2007, **76**, 014113.
13 M. I. Eremets, A. G. Gavrilruk, I. A. Trojan, D. A. Dzivenko and R. Boehler, *Nat. Mater.*, 2004, **3**, 558–563.
14 C. Mailhiot, L. H. Yang and A. K. McMahan, *Phys. Rev. B: Condens. Matter Mater. Phys.*, 1992, **46**, 14419–14435.
15 V. E. Zarko, *Combust., Explos. Shock Waves*, 2010, **46**, 121–131.
16 M. Ceppatelli, R. Bini and V. Schettino, *Proc. Natl. Acad. Sci. U. S. A.*, 2009, **106**, 1454–1459.
17 J. A. Ciezak-Jenkins, B. A. Steele, G. M. Borstad and I. I. Oleynik, *J. Chem. Phys.*, 2017, **146**, 184309.
18 R. L. Mills, B. Olinger and D. T. Cromer, *J. Chem. Phys.*, 1986, **84**, 2837–2845.
19 M. Kima and C. S. Yoo, *J. Chem. Phys.*, 2011, **134**, 044519.
20 M. Noyman, S. Zilberg and Y. J. Haas, *J. Phys. Chem. A*, 2009, **113**, 7376–7382.
21 K. D. Colvin and D. L. Strout, *J. Phys. Chem. A*, 2005, **109**, 8011–8015.
22 C. S. Yoo, M. Kim, J. Lim, Y. J. Ryu and I. G. Batyrev, *J. Phys. Chem. C*, 2018, **122**, 13054–13060.
23 M. Ceppatelli, M. Pagliai, R. Bini and H. J. Jodl, *J. Phys. Chem. C*, 2015, **119**, 130–140.
24 D. K. Spaulding, G. Weck, P. Loubeyre, F. Datchi, P. Dumas and M. Hanfland, *Nat. Commun.*, 2014, **5**, 5739.
25 T. M. Klapotke, M. Stein and J. Z. Stierstorfer, *Anorg. Allg. Chem.*, 2008, **634**, 1711–1723.
26 W. Li, X. Huang, K. Bao, Z. Zhao, Y. Huang, L. Wang, G. Wu, B. Zhou, D. Duan, F. Li, Q. Zhou, B. Liu and T. Cui, *Sci. Rep.*, 2017, **7**, 39249.
27 C. Jin, Y. Liu, L. Wang, W. Zhang, T. Zhang and J. Zhu, *RSC Adv.*, 2020, **10**, 30069–30076.
28 J. A. Ciezak, *Propellants, Explos., Pyrotech.*, 2010, **35**, 373–378.
29 H. K. Mao, J. Xu and P. M. Bell, *J. Geophys. Res.*, 1986, **91**, 4673–4676.
30 C. Prescher and V. B. Prakapenka, *High Pressure Res.*, 2015, **35**, 223–230.
31 F. Billes, H. Endredi and G. Keresztury, *THEOCHEM*, 2000, **530**, 183–200.
32 T. Hattori, A. Sano-Furukawa, H. Arima, K. Komatsu, A. Yamada, Y. Inamura, T. Nakatani, Y. Seto, T. Nagai, W. Utsumi, T. Iitaka, H. Kagi, Y. Katayama, T. Inoue, T. Otomo, K. Suzuya, T. Kamiyama, M. Arai and T. Yagi, *Nucl. Instrum. Methods Phys. Res., Sect. A*, 2015, **780**, 55–67.
33 T. Hattori, A. Sano-Furukawa, S. Machida, J. Abe, K. Funakoshi, H. Arima and N. Okazaki, *High Pressure Res.*, 2019, **39**, 417–425.
34 V. Petricek, M. Dusek and L. Palatinus, *Z. Kristallogr.*, 2014, **229**, 345–352.
35 J. P. Perdew, K. Burke and M. Ernzerhof, *Phys. Rev. Lett.*, 1996, **77**, 3865–3868.
36 S. J. Clark, M. D. Segall, C. J. Pickard, P. J. Hasnip, M. J. Probert, K. Refson and M. C. Payne, *Z. Kristallogr.*, 2005, **220**, 567–570.
37 S. Baroni, S. D. Gironcoli, A. D. Corso and P. Giannozzi, *Rev. Mod. Phys.*, 2001, **73**, 515–562.
38 T. Arias, M. C. Payne and J. D. Joannopoulos, *Phys. Rev. Lett.*, 1992, **69**, 1077–1080.
39 H. C. Andersen, *J. Chem. Phys.*, 1980, **72**, 2384–2393.
40 D. R. Hamann, M. Schluter and C. Chiang, *Phys. Rev. Lett.*, 1979, **43**, 1494–1497.
41 A. Tkatchenko and M. Scheffler, *Phys. Rev. Lett.*, 2009, **102**, 073005.
42 R. Goddard, O. Heinemann and C. Kruger, *Acta Crystallogr., Sect. C: Cryst. Struct. Commun.*, 1997, **53**, 590–592.
43 F. Birch, *Phys. Rev.*, 1947, **71**, 809–824.
44 F. Birch, *J. Geophys. Res.-Atmos.*, 1978, **83**, 1257–1268.
45 Y. Zhao and I. L. Spain, *Phys. Rev. B: Condens. Matter Mater. Phys.*, 1989, **40**, 993–997.
46 J. K. Cockcroft, A. Rosu-Finsen, A. N. Fitch and J. H. Williams, *CrystEngComm*, 2018, **20**, 6677–6682.
47 Y. Wang, X. Dong, X. Tang, H. Zheng, K. Li, X. Lin, L. Fang, G. Sun, X. Chen, L. Xie, C. L. Bull, N. P. Funnell, T. Hattori, A. Sano-Furukawa, J. Chen, D. K. Hensley, G. Cody, Y. Ren, H. H. Lee and H. K. Mao, *Angew. Chem., Int. Ed.*, 2019, **58**, 1468–1473.
48 J. Sun, X. Dong, Y. Wang, K. Li, H. Zheng, L. Wang, G. D. Cody, C. A. Tulk, J. J. Molaison, X. Lin, Y. Meng, C. Jin and H. K. Mao, *Angew. Chem., Int. Ed.*, 2017, **56**, 6553–6557.
49 L. Wang, X. Dong, Y. Wang, H. Zheng, K. Li, X. Peng, H. K. Mao, C. Jin, Y. Meng, M. Huang and Z. Zhao, *J. Phys. Chem. Lett.*, 2017, **8**, 4241–4245.
50 J. Han, X. Tang, Y. Wang, Y. Wang, Y. Han, X. Lin, X. Dong, H. H. Lee, H. Zheng, K. Li and H. K. Mao, *J. Phys. Chem. C*, 2019, **123**, 30746–30753.

